Computational Mechanics 28 (2002) 489–504 © Springer-Verlag 2002
DOI 10.1007/s00466-002-0314-2

A virtual work derivation of the scaled boundary finite-element method for elastostatics

A. J. Deeks, J. P. Wolf

Abstract The scaled-boundary finite element method is a novel semi-analytical technique, combining the advantages of the finite element and the boundary element methods with unique properties of its own. This paper develops a new virtual work formulation and modal interpretation of the method for elastostatics. This formulation follows a similar procedure to the traditional virtual work derivation of the standard finite element method. As well as making the method more accessible, this approach leads to new techniques for the treatment of body loads, side-face loads and axisymmetry that simplify implementation. The paper fully develops the new formulation, and provides four examples illustrating the versatility, accuracy and efficiency of the scaled boundary finite-element method. Both bounded and unbounded domains are treated, together with problems involving stress singularities.

Keywords Scaled boundary finite-element method, Plane stress, Plane strain, Axisymmetry, Unbounded domain, Stress singularity

1 Introduction

The scaled boundary finite-element method is a novel semi-analytical approach to continuum analysis developed by Wolf and Song. The method was originally derived to compute the dynamic stiffness of an unbounded domain (Wolf and Song, 1996a), and was based on a 'cloning' technique in which the analytical limit was taken as the width of the cloned cell (the infinitesimal finite-element cell) tended to zero. This derivation is referred to as the mechanically-based derivation. The method has proved to be more general than initially envisaged, with later developments allowing analysis of incompressible material and bounded domains (Wolf and Song, 1996b), and the inclusion of body loads (Song and Wolf, 1999). The complexity of the original derivation of the technique led to the development of a weighted residual formulation (Song and Wolf, 1997; Wolf and Song, 2001). However, this formulation is still significantly more complex than comparable derivations of the finite element method.

This paper attempts to increase the penetration of the method into the general field of computational mechanics, and in particular structural mechanics. To do this it provides a new virtual work formulation and modal interpretation of the scaled boundary finite-element method for elastostatics, developed along similar lines to the classical virtual work formulation of the finite element method. This formulation not only makes the method more approachable to the wider engineering science community, but also leads to new techniques for the treatment of body loads, side-face loads and axisymmetry which simplify implementation. Unlike the weighted residual formulation, the virtual work approach does not require the introduction of identities established by observation, and the equivalent nodal boundary forces are obtained directly from the virtual work statement.

Although it may be noted that the virtual work principle can be expressed as an equivalent weighted residual statement (Zienkiewicz, 1977), not every weighted residual statement may be interpreted as a virtual work equation. The virtual work derivation presented in this paper is not equivalent to the existing weighted residual formulation of the scaled boundary finite-element method, although the final scaled boundary finite-element equations in displacement are identical to those obtained by the weighted residual and the mechanically-based formulations.

The paper also discusses the unique advantages of the scaled boundary finite-element method for elastostatic problems, and presents examples demonstrating excellent performance of the technique in comparison with finite element analysis.

This paper commences with a virtual work development of the standard finite element method for two-dimensional problems of elastostatics. This section is included to introduce notation and to provide a point of reference for readers unfamiliar with the scaled boundary finite-element method. A virtual work derivation of the scaled boundary finite-element method for the same types of problems is developed in full, and the inclusion of body loads and side-face loads is addressed. The derivation is then extended to axisymmetric situations. The advantages of the scaled boundary finite-element method for problems of elastostatics are detailed, and the use of sub-structuring techniques to maximise these advantages is discussed. Four

Received 20 May 2001 / Accepted 1 February 2002

A. J. Deeks (✉)
Department of Civil Engineering,
The University of Western Australia,
Crawley, Western Australia 6009, Australia
e-mail: deeks@civil.uwa.edu.au

J. P. Wolf
Department of Civil Engineering,
Institute of Hydraulics and Energy,
Swiss Federal Institute of Technology Lausanne,
CH-1015 Lausanne, Switzerland

examples are then provided demonstrating the versatility, accuracy and efficiency of the scaled boundary finite-element method. The examples are also solved using standard finite element techniques, and the results compared.

2 Finite element approximation

In the following two sections the analysis of a two-dimensional elastostatic problem is considered for simplicity. The equations and arguments can be extended easily to three dimensions. Enforcing internal equilibrium leads to the differential equation

$$[L]^{\mathrm{T}}\{\sigma(x,y)\} = \{p(x,y)\} \tag{1}$$

which must be satisfied at every point within the domain ("volume" V). Here $\{p(x,y)\}$ is the body load and $[L]$ is the linear operator relating the strains $\{\varepsilon(x,y)\}$ and the displacements $\{u(x,y)\}$

$$\{\varepsilon(x,y)\} = [L]\{u(x,y)\} \tag{2}$$

The stresses and strains are related by the elasticity matrix $[D]$

$$\{\sigma(x,y)\} = [D]\{\varepsilon(x,y)\} \tag{3}$$

The boundary S can be represented by a set of points $(x_0 + x_s(s), y_0 + y_s(s))$, where s is the boundary coordinate, measuring the distance around the boundary to the point, and (x_0, y_0) is a point introduced to simplify construction of $x_s(s)$ and $y_s(s)$. Boundary conditions must be specified at all points on either displacements or surface tractions. Boundary conditions are formulated on displacements as

$$\{u(s)\} = \{\bar{u}(s)\} \quad \text{on } S_u \tag{4}$$

and on surface tractions as

$$\{t(s)\} = \{\bar{t}(s)\} \quad \text{on } S_t \tag{5}$$

Definitions of the vector components, the linear operator and the elasticity matrices for problems of plane stress, plane strain and axisymmetry are given in Appendix A.

The task is to find a displacement field $\{u(x,y)\}$ which satisfies Eqs. (1), (2) and (3) everywhere within domain V, and satisfies Eqs. (4) and (5) on the boundary S. For most problems this is not possible, and an approximate solution must be found.

An alternative formulation of the equilibrium requirement is the virtual work statement. Using $\{\delta u(x,y)\}$ to represent a virtual displacement field, and

$$\{\delta\varepsilon(x,y)\} = [L]\{\delta u(x,y)\} \tag{6}$$

to represent the corresponding virtual strains, the virtual work equation states that

$$\int_V \{\delta\varepsilon(x,y)\}^{\mathrm{T}}\{\sigma(x,y)\}\mathrm{d}V - \int_S \{\delta u(s)\}^{\mathrm{T}}\{t(s)\}\mathrm{d}s - \int_V \{\delta u(x,y)\}^{\mathrm{T}}\{p(x,y)\}\mathrm{d}V = 0 \tag{7}$$

The first term is the internal virtual work, the second term is the external virtual work done by the boundary tractions evaluated over the entire boundary, and the third term is the external virtual work done by the body loads. If this equation is satisfied for all virtual displacement fields, equilibrium is satisfied in the strong sense. If it is satisfied for a subset of virtual displacement fields, equilibrium is only satisfied in a weak sense.

The finite element method seeks an approximate solution for $\{u(x,y)\}$ as a linear combination of n predetermined shape functions $N_i(x,y)$, where n is a finite number.

$$\{u_h(x,y)\} = \sum_{i=1}^{n} N_i(x,y)u_{hi} = [N(x,y)]\{u_h\} \tag{8}$$

In the standard finite element approach, the shape functions have unit value at a particular node and zero value at all other nodes. In this case $\{u_h\}$ can be identified as the nodal displacements.

The strains associated with the approximate displacement field will be

$$\{\varepsilon_h(x,y)\} = [L]\{u_h(x,y)\} = [L][N(x,y)]\{u_h\} = [B(x,y)]\{u_h\} \tag{9}$$

where, for convenience, the strain-nodal displacement matrix is introduced as

$$[B(x,y)] = [L][N(x,y)] \tag{10}$$

The approximate stresses are then

$$\{\sigma_h(x,y)\} = [D]\{\varepsilon_h(x,y)\} = [D][B(x,y)]\{u_h\} \tag{11}$$

Since, in general, the shape functions do not satisfy the governing differential equation, these stresses will not normally satisfy internal equilibrium at any point. The virtual work statement can be used to require that equilibrium is at least satisfied in a weak sense. An approximate solution consisting of a linear combination of n shape functions can be made to satisfy the virtual work equation for a virtual displacement space spanned by n independent virtual displacement fields. The Galerkin approach uses the same shape functions used to construct $\{u_h(x,y)\}$ to provide the n independent virtual displacement fields. In this case the virtual work equation must be satisfied for any linear combination of the shape functions. Denoting the virtual nodal displacements by $\{\delta u\}$, this means that the virtual work equation must be satisfied for all virtual displacement fields represented by

$$\{\delta u(x,y)\} = [N(x,y)]\{\delta u\} \tag{12}$$

and the corresponding virtual strain fields

$$\{\delta\varepsilon(x,y)\} = [L][N(x,y)]\{\delta u\} = [B(x,y)]\{\delta u\} \tag{13}$$

Substituting Eqs. (11), (12) and (13) into (7), the virtual work equation becomes

$$\{\delta u\}^{\mathrm{T}}\left[\int_V [B(x,y)]^{\mathrm{T}}[D][B(x,y)]\{u_h\}\mathrm{d}V - \int_S [N(s)]^{\mathrm{T}}\{t(s)\}\mathrm{d}s - \int_V [N(x,y)]^{\mathrm{T}}\{p(x,y)\}\mathrm{d}V\right] = 0 \tag{14}$$

In order that the equation be satisfied for any choice of $\{\delta u\}$

$$[K_s]\{u_h\} - \{P\} = \{0\} \tag{15}$$

must apply, where the stiffness matrix

$$[K_s] = \int_V [B(x,y)]^{\mathrm{T}}[D][B(x,y)]\mathrm{d}V \tag{16}$$

and the equivalent nodal forces are

$$\{P\} = \int_S [N(s)]^{\mathrm{T}}\{t(s)\}\mathrm{d}s + \int_V [N(x,y)]^{\mathrm{T}}\{p(x,y)\}\mathrm{d}V \tag{17}$$

Prescribed boundary displacement conditions constrain some $\{u_h\}$ terms, while prescribed boundary tractions constrain some $\{P\}$ terms. The number of constrained $\{u_h\}$ terms and unknown $\{P\}$ terms are equal. Equation (15) is thus a set of n linear equations in n unknowns, which can be solved for the unknown nodal displacements and the unknown integrated boundary tractions (equivalent nodal reaction forces). The entire approximate displacement field is obtained from Eq. (8). The strain and stress fields are then given by Eqs. (9) and (11) respectively.

Note that the finite element method only satisfies equilibrium in a weak sense. The correct solution to a problem will only be found if that solution lies within the solution space spanned by the shape functions. If this is not the case, the computed stress field will violate equilibrium at every point. As the number of elements in the model is increased, the solution space spanned by the shape functions increases, and the degree to which equilibrium is violated is reduced. Typically the shape functions are polynomials. If the exact solution to a problem is smooth and continuous, a good approximation to the solution may be found using the finite element method. However, many problems of structural mechanics involve domains with sharp corners, and with supports and loads applied over small portions of the boundary. In general, the stress field in a finite element model of a continuum with a point load or point support will not converge at these points. The standard finite element method does not deal well with problems involving stress singularities or unbounded domains. Never-the-less, 'work-around' techniques employing shape functions selected with a priori knowledge of the expected form of the solution, such as singularity elements (Benzley, 1974) and infinite elements (Bettess, 1977), allow such problems to be tackled in a finite element context.

A major strength of the finite element method is the ease with which complex geometries, anisotropic materials and boundary conditions can be handled.

3
Scaled boundary finite-element approximation

3.1
Formulation

The scaled boundary finite-element method is formulated to take advantage of analytical techniques available to solve ordinary differential equations. (Many one-dimensional problems of elastostatics can be solved analytically using the governing equations, without introducing the errors implicit in the use of finite elements. One example is the bending of a uniform beam under a distributed load.)

Instead of using virtual work to reduce the non-homogeneous set of governing partial differential equations to a set of linear equations (as in the finite element method), the scaled boundary finite-element method reduces the governing partial differential equations to a set of ordinary linear differential equations, which can be solved analytically. The resulting equations represent a stronger equilibrium requirement than the linear finite element equations. The reduction is accomplished by introducing shape functions in one coordinate direction, while working analytically in the other direction. To allow simple incorporation of arbitrary boundary geometries and discontinuous boundary conditions, it is advantageous to discretise the boundary. The two goals are achieved simultaneously by using a coordinate system in which one coordinate runs around the boundary.

The scaled boundary finite-element method introduces such a coordinate system by scaling the domain boundary relative to a scaling centre (x_0, y_0) selected within the domain (Fig. 1). The normalised radial coordinate ξ runs from the scaling centre towards the boundary, and has values of zero at the scaling centre and unity at the boundary. The other circumferential coordinate s specifies a distance around the boundary from an origin on the boundary. The scaled boundary and Cartesian coordinate systems are related by the scaling equations

$$x = x_0 + \xi x_s(s) \tag{18a}$$

$$y = y_0 + \xi y_s(s) \tag{18b}$$

Displacement and stress components are retained in the original Cartesian coordinate directions, while position is specified in terms of the scaled boundary coordinates. An approximate solution is sought in the form

$$\{u_h(\xi,s)\} = \sum_{i=1}^{n}[N_i(s)]u_{hi}(\xi) = [N(s)]\{u_h(\xi)\} \tag{19}$$

This represents a discretisation of the boundary $\xi = 1$ with the shape functions $[N(s)]$. The unknown vector $\{u_h(\xi)\}$ is a set of n functions analytical in ξ. The same shape functions apply for all lines with a constant ξ.

Mapping the linear operator to the scaled boundary coordinate system using standard methods (see Appendix B)

$$[L] = [L^1]\frac{\partial}{\partial x} + [L^2]\frac{\partial}{\partial y} = [b^1(s)]\frac{\partial}{\partial \xi} + \frac{1}{\xi}[b^2(s)]\frac{\partial}{\partial s} \tag{20}$$

where $[b^1(s)]$ and $[b^2(s)]$ are dependent only on the boundary definition (see Eqs. (B9) and (B10)).

Combining Eqs. (2) and (3) and substituting Eq. (20), the approximate stresses are

$$\begin{aligned}\{\sigma_h(\xi,s)\} &= [D]\{\varepsilon_h(\xi,s)\} \\ &= [D][B^1(s)]\{u_h(\xi)\}_{,\xi} + \frac{1}{\xi}[D][B^2(s)]\{u_h(\xi)\}\end{aligned} \tag{21}$$

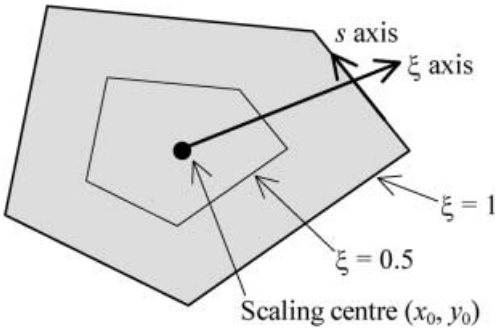

Fig. 1. Definition of the scaled boundary coordinate system

where, for convenience

$$[B^1(s)] = [b^1(s)][N(s)] \tag{22}$$

$$[B^2(s)] = [b^2(s)][N(s)]_{,s} \tag{23}$$

As in the finite element method, the virtual work statement is applied to introduce the equilibrium requirement. A virtual displacement field is formed using the shape functions $[N(s)]$ to interpolate between the nodes in the circumferential direction (the Galerkin approach). This virtual displacement field is of the form (analogous to Eq. (19))

$$\{\delta u(\xi, s)\} = [N(s)]\{\delta u(\xi)\} \tag{24}$$

where $\{\delta u(\xi)\}$ contains n functions describing the variation of the virtual displacements in the radial direction, and $\{\delta u(\xi = 1)\}$ contains the virtual nodal displacements. The corresponding virtual strain field is of the form (analogous to Eq. (21))

$$\{\delta\varepsilon(\xi, s)\} = [B^1(s)]\{\delta u(\xi)\}_{,\xi} + \frac{1}{\xi}[B^2(s)]\{\delta u(\xi)\} \tag{25}$$

Note from equation (B6) that

$$\mathrm{d}V = |J|\xi \, \mathrm{d}\xi \, \mathrm{d}s \tag{26}$$

where $|J|$ is the Jacobian at the boundary ($\xi = 1$).

The case where there is no body load present will be considered first. In this case the virtual work statement (Eq. (7)) becomes

$$\int_V \{\delta\varepsilon(\xi, s)\}^{\mathrm{T}}\{\sigma_h(\xi, s)\}\mathrm{d}V - \int_S \{\delta u(s)\}^{\mathrm{T}}\{t(s)\}\mathrm{d}s = 0 \tag{27}$$

where the first term represents the internal work and the second term the external work.

Substituting Eqs. (21), (25) and (26), the internal virtual work term is expanded as follows:

$$\begin{aligned}
&\int_V \{\delta\varepsilon(\xi, s)\}^{\mathrm{T}}\{\sigma_h(\xi, s)\}\mathrm{d}V \\
&= \int_V \left[[B^1(s)]\{\delta u(\xi)\}_{,\xi} + \frac{1}{\xi}[B^2(s)]\{\delta u(\xi)\}\right]^{\mathrm{T}} \\
&\quad \times \left[[D][B^1(s)]\{u_h(\xi)\}_{,\xi} + \frac{1}{\xi}[D][B^2(s)]\{u_h(\xi)\}\right]\mathrm{d}V \\
&= \int_S \int_0^1 \{\delta u(\xi)\}_{,\xi}^{\mathrm{T}}[B^1(s)]^{\mathrm{T}}[D][B^1(s)]\xi\{u_h(\xi)\}_{,\xi}|J|\mathrm{d}\xi \, \mathrm{d}s \\
&\quad + \int_S \int_0^1 \{\delta u(\xi)\}_{,\xi}^{\mathrm{T}}[B^1(s)]^{\mathrm{T}}[D][B^2(s)]\{u_h(\xi)\}|J|\mathrm{d}\xi \, \mathrm{d}s \\
&\quad + \int_S \int_0^1 \{\delta u(\xi)\}^{\mathrm{T}}[B^2(s)]^{\mathrm{T}}[D][B^1(s)]\{u_h(\xi)\}_{,\xi}|J|\mathrm{d}\xi \, \mathrm{d}s \\
&\quad + \int_S \int_0^1 \{\delta u(\xi)\}^{\mathrm{T}}[B^2(s)]^{\mathrm{T}}[D][B^2(s)]\frac{1}{\xi}\{u_h(\xi)\}|J|\mathrm{d}\xi \, \mathrm{d}s
\end{aligned} \tag{28}$$

The area integrals containing $\{\delta u(\xi)\}_{,\xi}$ are integrated with respect to ξ using Green's Theorem, introducing line integrals evaluated around the boundary and leading to

$$\begin{aligned}
&\int_V \{\delta\varepsilon(\xi, s)\}^{\mathrm{T}}\{\sigma_h(\xi, s)\}\mathrm{d}V \\
&= \int_S \{\delta u(\xi)\}^{\mathrm{T}}[B^1(s)]^{\mathrm{T}}[D][B^1(s)]\xi\{u_h(\xi)\}_{,\xi}|J|\mathrm{d}s\Big|_{\xi=1} \\
&\quad - \int_S \int_0^1 \{\delta u(\xi)\}^{\mathrm{T}}[B^1(s)]^{\mathrm{T}}[D][B^1(s)] \\
&\quad \times \{\{u_h(\xi)\}_{,\xi} + \xi\{u_h(\xi)\}_{,\xi\xi}\}|J|\mathrm{d}\xi \mathrm{d}s \\
&\quad + \int_S \{\delta u(\xi)\}^{\mathrm{T}}[B^1(s)]^{\mathrm{T}}[D][B^2(s)]\{u_h(\xi)\}|J|\mathrm{d}s\Big|_{\xi=1} \\
&\quad - \int_S \int_0^1 \{\delta u(\xi)\}^{\mathrm{T}}[B^1(s)]^{\mathrm{T}}[D][B^2(s)]\{u_h(\xi)\}_{,\xi}|J|\mathrm{d}\xi \mathrm{d}s \\
&\quad + \int_S \int_0^1 \{\delta u(\xi)\}^{\mathrm{T}}[B^2(s)]^{\mathrm{T}}[D][B^1(s)]\{u_h(\xi)\}_{,\xi}|J|\mathrm{d}\xi \mathrm{d}s \\
&\quad + \int_S \int_0^1 \{\delta u(\xi)\}^{\mathrm{T}}[B^2(s)]^{\mathrm{T}}[D][B^2(s)]\frac{1}{\xi}\{u_h(\xi)\}|J|\mathrm{d}\xi \mathrm{d}s
\end{aligned} \tag{29}$$

For convenience the following coefficient matrices are introduced

$$[E^0] = \int_S [B^1(s)]^{\mathrm{T}}[D][B^1(s)]|J|\mathrm{d}s \tag{30a}$$

$$[E^1] = \int_S [B^2(s)]^{\mathrm{T}}[D][B^1(s)]|J|\mathrm{d}s \tag{30b}$$

$$[E^2] = \int_S [B^2(s)]^{\mathrm{T}}[D][B^2(s)]|J|\mathrm{d}s \tag{30c}$$

These integrals can be computed element by element over the boundary, and assembled together for the entire boundary in the same manner as the stiffness matrix is determined for the entire domain in the standard finite element method.

Using $\{u_h\}$ to represent $\{u_h(\xi = 1)\}$ and so forth, Eq. (29) is expressed succinctly as

$$\int_V \{\delta\varepsilon(\xi,s)\}^{\mathrm{T}}\{\sigma_h(\xi,s)\}\mathrm{d}V = \{\delta u\}^{\mathrm{T}}\{[E^0]\{u_h\}_{,\xi} + [E^1]^{\mathrm{T}}\{u_h\}\} - \int_0^1 \{\delta u(\xi)\}^{\mathrm{T}}\Big\{[E^0]\xi\{u_h(\xi)\}_{,\xi\xi} + [[E^0] + [E^1]^{\mathrm{T}} - [E^1]]\{u_h(\xi)\}_{,\xi} - [E^2]\frac{1}{\xi}\{u_h(\xi)\}\Big\}\mathrm{d}\xi \quad (31)$$

On substitution of Eq. (24), the external virtual work term in Eq. (27) becomes

$$\int_S \{\delta u(s)\}^{\mathrm{T}}\{t(s)\}\mathrm{d}s = \{\delta u\}^{\mathrm{T}}\int_S \{N(s)\}^{\mathrm{T}}\{t(s)\}\mathrm{d}s \quad (32)$$

By comparison with Eq. (17), the integral on the right-hand side of Eq. (32) can be identified as the equivalent nodal forces due to the boundary tractions, $\{P\}$. The complete virtual work equation becomes

$$\{\delta u\}^{\mathrm{T}}\{[E^0]\{u_h\}_{,\xi} + [E^1]^{\mathrm{T}}\{u_h\}\} - \{\delta u\}^{\mathrm{T}}\{P\} - \int_0^1 \{\delta u(\xi)\}^{\mathrm{T}}\Big\{[E^0]\xi\{u_h(\xi)\}_{,\xi\xi} + [[E^0] + [E^1]^{\mathrm{T}} - [E^1]]\{u_h(\xi)\}_{,\xi} - [E^2]\frac{1}{\xi}\{u_h(\xi)\}\Big\}\mathrm{d}\xi = \{0\} \quad (33)$$

In order for Eq. (33) to be satisfied for all $\{\delta u(\xi)\}$ (implying that equilibrium is closely satisfied in the radial direction and in the finite element sense in the circumferential direction), both of the following conditions must be satisfied.

$$\{P\} = [E^0]\{u_h\}_{,\xi} + [E^1]^{\mathrm{T}}\{u_h\} \quad (34)$$

$$[E^0]\xi^2\{u_h(\xi)\}_{,\xi\xi} + [[E^0] + [E^1]^{\mathrm{T}} - [E^1]]\xi\{u_h(\xi)\}_{,\xi} - [E^2]\{u_h(\xi)\} = \{0\} \quad (35)$$

Equation (35) is the scaled boundary finite-element equation in displacement, which is derived in earlier work, both by a mechanically-based method (Wolf and Song, 1996b) and by a weighted residual method (Song and Wolf, 1997). Effectively the governing equations have been weakened in the circumferential direction in a finite element manner, but remain strong in the radial direction.

3.2 Solution procedure

By inspection, solutions to the homogeneous set of Euler–Cauchy differential equations represented by Eq. (35) must be of the form

$$\{u_h(\xi)\} = c_1\xi^{-\lambda_i}\{\phi_1\} + c_2\xi^{-\lambda_2}\{\phi_2\} + \cdots \quad (36)$$

where the exponents $-\lambda_i$ and corresponding vectors $\{\phi_i\}$ may be interpreted as independent modes of deformation which closely satisfy internal equilibrium in the ξ direction. (The negative sign is adopted for consistency with earlier work (Wolf and Song, 1996b), in which the method is derived for unbounded domains.) The integration constants c_i represent the contribution of each mode to the solution, and are dependent on the boundary conditions.

The displacements for each mode take the form (omitting the subscript)

$$\{u(\xi)\} = \xi^{-\lambda}\{\phi\} \quad (37)$$

The vector $\{\phi\}$ can be identified as the modal displacements at the boundary nodes, while λ can be identified as a modal scaling factor for the 'radial' direction. Substituting this solution into Eq. (35) yields the quadratic eigenproblem

$$[\lambda^2[E^0] - \lambda[[E^1]^{\mathrm{T}} - [E^1]] - [E^2]]\{\phi\} = \{0\} \quad (38)$$

The equivalent nodal forces required at the boundary to equilibrate each displacement mode are obtained by substituting Eq. (37) into Eq. (34) (which is evaluated at $\xi = 1$) as

$$\{q\} = [[E^1]^{\mathrm{T}} - \lambda[E^0]]\{\phi\} \quad (39)$$

The quadratic eigenproblem can be converted to a standard linear eigenproblem at the expense of doubling the number of degrees of freedom. First, Eq. (39) is rearranged as follows:

$$\lambda\{\phi\} = [E^0]^{-1}[[E^1]^{\mathrm{T}}\{\phi\} - \{q\}] \quad (40)$$

Then, selectively substituting Eq. (40) into Eq. (38)

$$\lambda[E^0][E^0]^{-1}[[E^1]^{\mathrm{T}}\{\phi\} - \{q\}] - \lambda[E^1]^{\mathrm{T}}\{\phi\} + [E^1][E^0]^{-1}[[E^1]^{\mathrm{T}}\{\phi\} - \{q\}] - [E^2]\{\phi\} = \{0\} \quad (41)$$

or

$$\lambda\{q\} = [E^1][E^0]^{-1}[[E^1]^{\mathrm{T}}\{\phi\} - \{q\}] - [E^2]\{\phi\} \quad (42)$$

Assembling together the two sets of equations represented by Eqs. (40) and (42) the problem is now in linear form

$$\begin{bmatrix} [E^0]^{-1}[E^1]^{\mathrm{T}} & -[E^0]^{-1} \\ [E^1][E^0]^{-1}[E^1]^{\mathrm{T}} - [E^2] & -[E^1][E^0]^{-1} \end{bmatrix}\begin{Bmatrix}\phi \\ q\end{Bmatrix} = \lambda\begin{Bmatrix}\phi \\ q\end{Bmatrix} \quad (43)$$

Solution of this standard eigenproblem yields $2n$ modes. The eigenvectors contain the modal displacements and the equivalent modal node forces. For a bounded domain only the modes with non-positive real components of λ lead to finite displacements at the scaling centre (Eq. (37) with

$\xi = 0$). This subset of n modal displacements is designated by $[\Phi_1]$, where the vectors in the set form the columns of the matrix. The subset of modal force vectors corresponding to the n modes in $[\Phi_1]$ is denoted as $[Q_1]$.

For any set of boundary node displacements $\{u_h\}$, the integration constants required to satisfy Eq. (36) on the boundary ($\xi = 1$) are

$$\{c\} = [\Phi_1]^{-1}\{u_h\} \tag{44}$$

The equivalent nodal forces required to cause these displacements are

$$\{P\} = [Q_1]\{c\} = [Q_1][\Phi_1]^{-1}\{u_h\} \tag{45}$$

The stiffness matrix of the domain is therefore

$$[K] = [Q_1][\Phi_1]^{-1} \tag{46}$$

and the equilibrium requirement is reduced to

$$[K]\{u_h\} - \{P\} = \{0\} \tag{47}$$

Boundary conditions place constraints on subsets of $\{u_h\}$ and $\{P\}$, and the solution proceeds in the same manner as in standard finite element analysis. However, unlike that method, only boundary degrees of freedom are present.

The integration constants are then obtained using Eq. (44) and the displacement field is recovered by combining Eqs. (19) and (36) as

$$\{u_h(\xi, s)\} = [N(s)] \sum_{i=1}^{n} c_i \xi^{-\lambda_i} \{\phi_i\} \tag{48}$$

The stress field is obtained by substituting Eq. (48) into (21) as

$$\{\sigma_h(\xi, s)\} = [D] \sum_{i=1}^{n} c_i \xi^{-\lambda_i - 1} [-\lambda_i [B^1(s)] + [B^2(s)]] \{\phi_i\} \tag{49}$$

3.3 Side-faces

The above development assumes that the scaling centre is contained within a bounded solution domain. However, the formulation can also be applied when the scaling centre is selected to be on the boundary, provided the boundary is straight for a finite distance either side of the centre. (There can be a change in direction at the centre.) This is illustrated in Fig. 2. The two straight sections are termed side-faces.

The side-faces are described by constant values of s, s_0 and s_1. Since discretisation is only performed in the s direction, no discretisation is required on the side-faces. The boundary S in the equations in the preceeding sections is now used to represent the discretised boundary only. If necessary, zero displacement boundary conditions are applied over a side-face as a whole through the use of compatible shape functions $[N(s)]$. Zero surface traction side-face conditions are taken into account automatically, since they do not contribute work terms to Eq. (7). Non-zero surface tractions are discussed in Sect. 4. Constant displacement boundary conditions on the side-faces are satisfied exactly, while the traction boundary conditions are closely satisfied, without discretisation.

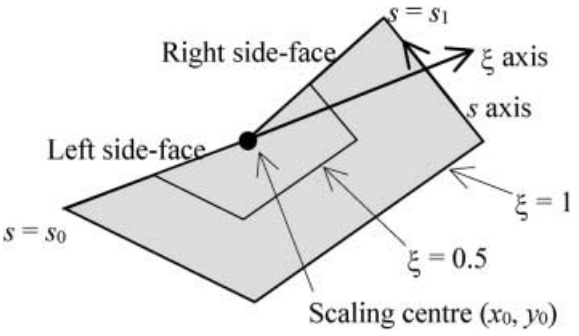

Fig. 2. Bounded domain with side-faces

3.4 Unbounded domains

An infinite domain containing a cavity can be represented by taking the range of ξ as from 1 to ∞ (Fig. 3a), and a semi-infinite domain can be modelled by including side-faces (Fig. 3b). In these cases, when the integration of the virtual work equation with respect to ξ is performed using Green's Theorem, the boundary is traversed in the opposite direction, changing the sign of the surface integral.

The virtual work statement then becomes

$$\{\delta u\}^{\mathrm{T}}\{-[E^0]\{u_h\}_{,\xi} - [E^1]^{\mathrm{T}}\{u_h\}\} - \{\delta u\}^{\mathrm{T}}\{P\} - \int_1^{\infty} \{\delta u(\xi)\}^{\mathrm{T}} \Big\{ [E^0]\xi\{u_h(\xi)\}_{,\xi\xi} + [[E^0] + [E^1]^{\mathrm{T}} - [E^1]]\{u_h(\xi)\}_{,\xi} - [E^2]\frac{1}{\xi}\{u_h(\xi)\} \Big\} \mathrm{d}\xi = \{0\} \tag{50}$$

which is satisfied for all $\{\delta u(\xi)\}$ when both

$$\{P\} = -[E^0]\{u_h\}_{,\xi} - [E^1]^{\mathrm{T}}\{u_h\} \tag{51}$$

and

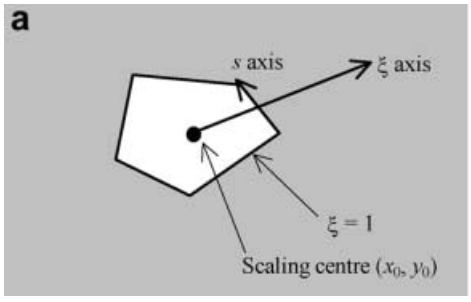

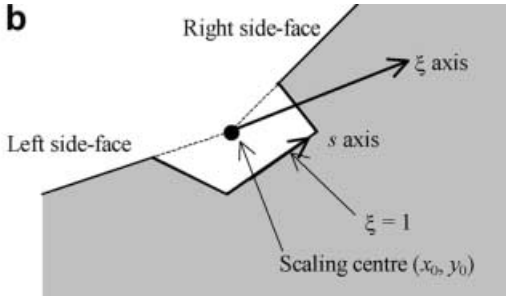

Fig. 3. Unbounded domains: **a** without side-faces; **b** with side-faces

$$[E^0]\xi^2\{u_h(\xi)\}_{,\xi\xi} + [[E^0] + [E^1]^{\mathrm{T}} - [E^1]]\xi\{u_h(\xi)\}_{,\xi} - [E^2]\{u_h(\xi)\} = \{0\} \quad (52)$$

Note that the scaled boundary finite-element equation in displacement (Eqs. (35) and (52)) is unchanged, while the sign of the equivalent nodal forces is reversed (Eqs. (34) and (51)). Solution of the quadratic eigenproblem (Eq. (38)) is therefore seen to yield a set of modes that span the solution spaces of both the bounded and unbounded domains simultaneously.

Consequently, the only difference in the solution procedure for unbounded domains arises after the modes are computed. For unbounded cases those modes with non-negative real components of λ are chosen as $[\Phi_2]$ to enforce finite displacements at infinity (Eq. (37) with $\xi \to \infty$). The corresponding nodal forces are $-[Q_2]$, where the negative sign is introduced due to the sign difference between Eqs. (34) and (51), and the stiffness matrix of the unbounded domain is

$$[K^\infty] = -[Q_2][\Phi_2]^{-1} \quad (53)$$

The rest of the solution proceeds as for the bounded domain.

4 Body loads and side-face loads

A non-zero body load creates an additional external virtual work term. For a bounded domain, this term may be expressed as

$$\int_V \{\delta u(\xi,s)\}^{\mathrm{T}}\{p(\xi,s)\}\mathrm{d}V = \int_0^1 \{\delta u(\xi)\}^{\mathrm{T}} \int_S [N(s)]^{\mathrm{T}}\{p(\xi,s)\}|J|\xi \mathrm{d}s\,\mathrm{d}\xi = \int_0^1 \{\delta u(\xi)\}^{\mathrm{T}}\xi\{F_b(\xi)\}\mathrm{d}\xi \quad (54)$$

where the equivalent nodal loads for the body loads are

$$\{F_b(\xi)\} = \int_S [N(s)]^{\mathrm{T}}\{p(\xi,s)\}|J|\mathrm{d}s \quad (55)$$

Similarly, non-zero tractions on the side-faces create additional external virtual work terms. It is possible to specify non-zero external line loads along each radial line corresponding to a boundary node, but this will not normally be realistic. The variation of the line loads in the ξ direction (specified in nodal degree of freedom directions) along all node lines may be represented by $\{F_t(\xi)\}$. Usually only the terms corresponding to the degrees of freedom of the side-face nodes will be non-zero. The line load magnitudes must be mapped from the dimensional radial coordinate to the dimensionless radial coordinate ξ in the usual way. The external virtual work done by the tractions on all the side-faces is then

$$\int_0^1 \{\delta u(\xi)\}^{\mathrm{T}}\{F_t(\xi)\}\mathrm{d}\xi \quad (56)$$

Including Eqs. (54) and (56) in the expanded virtual work equation (33) expands the scaled boundary finite-element equation in displacement to

$$[E^0]\xi^2\{u_h(\xi)\}_{,\xi\xi} + [[E^0] + [E^1]^{\mathrm{T}} - [E^1]]\xi\{u_h(\xi)\}_{,\xi} - [E^2]\{u_h(\xi)\} + \xi^2\{F_b(\xi)\} + \xi\{F_t(\xi)\} = \{0\} \quad (57)$$

A general solution to this non-homogeneous differential equation may be sought as a linear combination of the general solution of the homogeneous version (Eq. (35)) and particular solutions of the same form as the terms $\xi^2\{F_b(\xi)\}$ and $\xi\{F_t(\xi)\}$. Since the general solution of Eq. (35) is interpreted above as the combination of deformation modes, each of which closely satisfies internal equilibrium in the ξ direction, the additional solutions can also be interpreted as modes of deformation which almost satisfy internal equilibrium with the body loads and side-face loads respectively. The modes representing the general solution of Eq. (35) will be referred to as the 'homogeneous' modes, allowing differentiation between the mode types.

Many practical loads can be modelled as varying as a power function of the radial coordinate (such as constant or linearly varying distributed loads).

If the body load can be represented as

$$\{F_b(\xi)\} = \xi^b\{F_b\} \quad (58)$$

the body load mode displacements are of the form

$$\{u_b(\xi)\} = \xi^{b+2}\{\phi_b\} \quad (59)$$

Substitution of Eq. (59) into Eq. (57) (in the absence of side-face loads) yields

$$[(b+2)^2[E^0] + (b+2)[[E^1]^{\mathrm{T}} - [E^1]] - [E^2]]\{\phi_b\} + \{F_b\} = \{0\} \quad (60)$$

and the nodal displacements for the body load mode are obtained as

$$\{\phi_b\} = [(b+2)^2[E^0] + (b+2)[[E^1]^{\mathrm{T}} - [E^1]] - [E^2]]^{-1}\{-F_b\} \quad (61)$$

[If $-(b+2)$ corresponds to one of the eigenvalues of Eq. (38), the coefficient matrix will be singular. For practical implementation a small shift of the power will remove the singularity with negligible loss in accuracy.] The equivalent nodal forces on the discretised boundary in equilibrium with these displacements are obtained by substitution of Eq. (59) into Eq. (34) as

$$\{q_b\} = [(b+2)[E^0] + [E^1]^{\mathrm{T}}]\{\phi_b\} \quad (62)$$

If the side-face loads can also be represented as power functions of ξ such that

$$\{F_t(\xi)\} = \xi^t\{F_t\} \quad (63)$$

the side-face load mode displacements are of the form

$$\{u_t(\xi)\} = \xi^{t+1}\{\phi_t\} \tag{64}$$

Substitution of Eq. (64) into Eq. (57) (in the absence of body loads) yields

$$[(t+1)^2[E^0] + (t+1)[[E^1]^{\mathrm{T}} - [E^1]] - [E^2]]\{\phi_t\} + \{F_t\} = \{0\} \tag{65}$$

The nodal displacements for the side-face load mode can be obtained by rearrangement as

$$\{\phi_t\} = [(t+1)^2[E^0] + (t+1)[[E^1]^{\mathrm{T}} - [E^1]] - [E^2]]^{-1}\{-F_t\} \tag{66}$$

and the equivalent nodal boundary forces in equilibrium with these displacements by substitution of Eq. (64) into Eq. (34) as

$$\{q_t\} = [(t+1)[E^0] + [E^1]^{\mathrm{T}}]\{\phi_t\} \tag{67}$$

The complete solution (in the presence of body loads, side-face loads and boundary conditions applied along the discretised boundary) is now sought in the form

$$\{u_h(\xi,s)\} = [N(s)]\left(\xi^{b+2}\{\phi_b\} + \xi^{t+1}\{\phi_t\} + \sum_{i=1}^{n} c_i\xi^{-\lambda_i}\{\phi_i\}\right) \tag{68}$$

For a given set of integration constants, the displacements at the boundary nodes are

$$\{u_h\} = \{\phi_b\} + \{\phi_t\} + [\Phi_1]\{c\} \tag{69}$$

The equivalent nodal boundary forces in equilibrium with this displacement field are

$$\{P\} = \{q_b\} + \{q_t\} + [Q_1]\{c\} \tag{70}$$

Rearranging Eq. (69), the integration constants can be found in terms of the nodal displacements

$$\{c\} = [\Phi_1]^{-1}\{\{u_h\} - \{\phi_b\} - \{\phi_t\}\} \tag{71}$$

Substituting this equation into Eq. (69) and rearranging, the equilibrium requirement is reduced to

$$[Q_1][\Phi_1]^{-1}\{\{u_h\} - \{\phi_b\} - \{\phi_t\}\} = \{P\} - \{q_b\} - \{q_t\} \tag{72}$$

or

$$[K]\{u_h\} = \{P\} - \{q_b\} - \{q_t\} + [K]\{\{\phi_b\} + \{\phi_t\}\} \tag{73}$$

where

$$[K] = [Q_1][\Phi_1]^{-1} \tag{74}$$

as before (Eq. (46)). Boundary conditions on the discretised boundaries place constraints on subsets of $\{u_h\}$ and $\{P\}$ as before, and solution proceeds in the usual manner. Once the complete set of boundary displacements is found, Eq. (71) is used to obtain the integration constants. The displacement field is then recovered using Eq. (68), and the stress field is then obtained by substitution of this equation into Eq. (21) as

$$\{\sigma_h(\xi,s)\} = [D](\xi^{b+1}[(b+2)[B^1(s)] + [B^2(s)]]\{\phi_b\} + \xi^t[(t+1)[B^1(s)] + [B^2(s)]]\{\phi_t\}) + [D]\sum_{i=1}^{n} c_i\xi^{-\lambda_i-1}[-\lambda_i[B^1(s)] + [B^2(s)]]\{\phi_i\} \tag{75}$$

This modal treatment of body and side-face loads considerably simplifies implementation of the method, since during post-processing the body and side-face load modes can be treated in the same way as the homogeneous modes, with integration constants taken as unity during the computation of displacements and stresses.

5 Axisymmetry

The above derivations are limited to plane problems. Extension to axisymmetric situations is straightforward. Here the scaling centre is assumed to lie on the vertical axis of a cylindrical coordinate system (the z-axis) and the loading is assumed to be axisymmetric. The radial axis is taken to be r. This is illustrated in Fig. 4.

Equations (18)–(25) are unchanged, with the exception of the components of the stress and strain matrices, the linear operator and material matrices (which are provided in Appendix A), and the definition of $[B^2(s)]$, which becomes

$$[B^2(s)] = [b^2(s)][N(s)]_{,s} + [b^3(s)][N(s)] \tag{76}$$

with $[b^3(s)]$ defined in Eq. (B18). The infinitesimal volume is now

$$\mathrm{d}V = 2\pi r_s|J|\xi^2\,\mathrm{d}\xi\,\mathrm{d}s \tag{77}$$

where r_s is the radial coordinate of the boundary point ($\xi = 1, s$).

The internal virtual work term in Eq. (27) now becomes

$$\begin{aligned}\int_V \{\delta\epsilon(\xi,s)\}^{\mathrm{T}}\{\sigma_h(\xi,s)\}\mathrm{d}V &= \int_S\int_0^1 \{\delta u(\xi)\}_{,\xi}^{\mathrm{T}}[B^1(s)]^{\mathrm{T}}[D][B^1(s)]\xi^2\{u_h(\xi)\}_{,\xi}2\pi r_s|J|\mathrm{d}\xi\mathrm{d}s \\ &+ \int_S\int_0^1 \{\delta u(\xi)\}_{,\xi}^{\mathrm{T}}[B^1(s)]^{\mathrm{T}}[D][B^2(s)]\xi\{u_h(\xi)\}2\pi r_s|J|\mathrm{d}\xi\mathrm{d}s \\ &+ \int_S\int_0^1 \{\delta u(\xi)\}^{\mathrm{T}}[B^2(s)]^{\mathrm{T}}[D][B^1(s)]\xi\{u_h(\xi)\}_{,\xi}2\pi r_s|J|\mathrm{d}\xi\mathrm{d}s \\ &+ \int_S\int_0^1 \{\delta u(\xi)\}^{\mathrm{T}}[B^2(s)]^{\mathrm{T}}[D][B^2(s)]\{u_h(\xi)\}2\pi r_s|J|\mathrm{d}\xi\mathrm{d}s\end{aligned} \tag{78}$$

Integrating the terms containing $\{\delta u(\xi)\}_{,\xi}$ with respect to ξ using Green's theorem as before

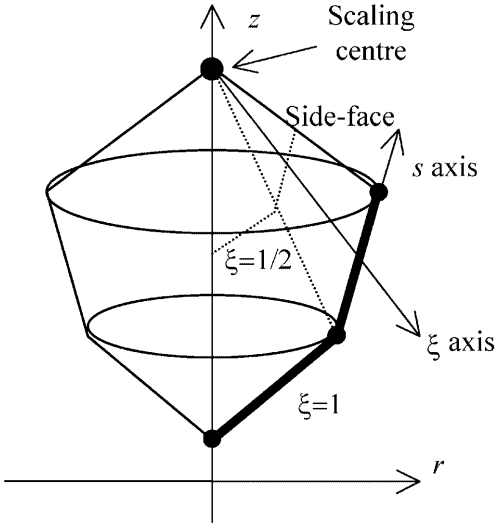

Fig. 4. Axisymmetric domain discretised with two linear elements

$$
\begin{aligned}
&\int_V \{\delta\varepsilon(\xi,s)\}^{\mathrm{T}}\{\sigma_h(\xi,s)\}\mathrm{d}V \\
&= \int_S \{\delta u(\xi)\}^{\mathrm{T}}[B^1(s)]^{\mathrm{T}}[D][B^1(s)]\xi^2\{u_h(\xi)\}_{,\xi}2\pi r_s|J|\mathrm{d}s\Big|_{\xi=1} \\
&\quad - \int_S\int_0^1 \{\delta u(\xi)\}^{\mathrm{T}}[B^1(s)]^{\mathrm{T}}[D][B^1(s)]\{2\xi\{u_h(\xi)\}_{,\xi} \\
&\quad + \xi^2\{u_h(\xi)\}_{,\xi\xi}\}2\pi r_s|J|\mathrm{d}\xi\mathrm{d}s \\
&\quad + \int_S \{\delta u(\xi)\}^{\mathrm{T}}[B^1(s)]^{\mathrm{T}}[D][B^2(s)]\xi\{u_h(\xi)\}2\pi r_s|J|\mathrm{d}s\Big|_{\xi=1} \\
&\quad - \int_S\int_0^1 \{\delta u(\xi)\}^{\mathrm{T}}[B^1(s)]^{\mathrm{T}}[D][B^2(s)]\{\{u_h(\xi)\} \\
&\quad + \xi\{u_h(\xi)\}_{,\xi}\}2\pi r_s|J|\mathrm{d}\xi\mathrm{d}s \\
&\quad + \int_S\int_0^1 \{\delta u(\xi)\}^{\mathrm{T}}[B^2(s)]^{\mathrm{T}}[D][B^1(s)]\xi\{u_h(\xi)\}_{,\xi}2\pi r_s|J|\mathrm{d}\xi\mathrm{d}s \\
&\quad + \int_S\int_0^1 \{\delta u(\xi)\}^{\mathrm{T}}[B^2(s)]^{\mathrm{T}}[D][B^2(s)]\{u_h(\xi)\}2\pi r_s|J|\mathrm{d}\xi\mathrm{d}s
\end{aligned}
\tag{79}
$$

The coefficient matrices now become

$$[E^0] = \int_S [B^1(s)]^{\mathrm{T}}[D][B^1(s)]2\pi r_s|J|\mathrm{d}s \tag{80a}$$

$$[E^1] = \int_S [B^2(s)]^{\mathrm{T}}[D][B^1(s)]2\pi r_s|J|\mathrm{d}s \tag{80b}$$

$$[E^2] = \int_S [B^2(s)]^{\mathrm{T}}[D][B^2(s)]2\pi r_s|J|\mathrm{d}s \tag{80c}$$

The external virtual work term in Eq. (27) becomes

$$\int_S \{\delta u(s)\}^{\mathrm{T}}\{t(s)\}\mathrm{d}s = \{\delta u\}^{\mathrm{T}}\int_S \{N(s)\}^{\mathrm{T}}\{t(s)\}2\pi r_s\,\mathrm{d}s \tag{81}$$

The integral on the right hand side of Eq. (81) can again be identified as the equivalent nodal forces due to the boundary tractions, $\{P\}$. The complete virtual work equation becomes

$$
\begin{aligned}
&\{\delta u\}^{\mathrm{T}}\{[E^0]\{u_h\}_{,\xi} + [E^1]^{\mathrm{T}}\{u_h\}\} - \{\delta u\}^{\mathrm{T}}\{P\} \\
&\quad - \int_0^1 \{\delta u(\xi)\}^{\mathrm{T}}\{[E^0]\xi^2\{u_h(\xi)\}_{,\xi\xi} \\
&\quad + [2[E^0] + [E^1]^{\mathrm{T}} - [E^1]]\xi\{u_h(\xi)\}_{,\xi} \\
&\quad - [[E^2] - [E^1]^{\mathrm{T}}]\{u_h(\xi)\}\}\mathrm{d}\xi = \{0\}\ .
\end{aligned}
\tag{82}
$$

Consequently, for axisymmetry, the equivalent nodal forces are still

$$\{P\} = [E^0]\{u_h\}_{,\xi} + [E^1]^{\mathrm{T}}\{u_h\} \tag{83}$$

while the scaled boundary finite-element equation in displacement becomes

$$
\begin{aligned}
&[E^0]\xi^2\{u_h(\xi)\}_{,\xi\xi} + [2[E^0] + [E^1]^{\mathrm{T}} - [E^1]]\xi\{u_h(\xi)\}_{,\xi} \\
&\quad - [[E^2] - [E^1]^{\mathrm{T}}]\{u_h(\xi)\} = \{0\}
\end{aligned}
\tag{84}
$$

Since only the coefficient matrices have changed, solutions to this equation are still of the form of Eq. (36). On substitution into Eq. (84), the quadratic eigenproblem becomes

$$
\begin{aligned}
&[\lambda^2[E^0] - \lambda[[E^0] + [E^1]^{\mathrm{T}} - [E^1]] \\
&\quad - [[E^2] - [E^1]^{\mathrm{T}}]]\{\phi\} = \{0\}
\end{aligned}
\tag{85}
$$

Since Eq. (83) still holds

$$\lambda\{\phi\} = [E^0]^{-1}[[E^1]^{\mathrm{T}}\{\phi\} - \{q\}] \tag{86}$$

Selectively substituting Eq. (86) into Eq. (85)

$$
\begin{aligned}
&\lambda[E^0][E^0]^{-1}[[E^1]^{\mathrm{T}}\{\phi\} - \{q\}] - \lambda[E^1]^{\mathrm{T}}\{\phi\} \\
&\quad + [[E^1] - [E^0]][E^0]^{-1}[[E^1]^{\mathrm{T}}\{\phi\} - \{q\}] \\
&\quad - [[E^2] - [E^1]^{\mathrm{T}}]\{\phi\} = \{0\}
\end{aligned}
\tag{87}
$$

or, using $[I]$ to represent the identity matrix

$$
\begin{aligned}
\lambda\{q\} &= [[E^1][E^0]^{-1}[E^1]^{\mathrm{T}} - [E^2]]\{\phi\} \\
&\quad + [[I] - [E^1][E^0]^{-1}]\{q\}
\end{aligned}
\tag{88}
$$

Assembling together the two sets of equations represented by Eqs. (86) and (88)

$$
\begin{bmatrix} [E^0]^{-1}[E^1]^{\mathrm{T}} & -[E^0]^{-1} \\ [E^1][E^0]^{-1}[E^1]^{\mathrm{T}} - [E^2] & [I] - [E^1][E^0]^{-1} \end{bmatrix}
\begin{Bmatrix} \phi \\ q \end{Bmatrix} = \lambda \begin{Bmatrix} \phi \\ q \end{Bmatrix}
\tag{89}
$$

The solution proceeds in the same manner as for plane stress and plane strain.

If body or side-face loads are present, the scaled boundary equation in displacement is

$$[E^0]\xi^2\{u_h(\xi)\}_{,\xi\xi} + [2[E^0] + [E^1]^{\mathrm{T}} - [E^1]]\xi\{u_h(\xi)\}_{,\xi} - [[E^2] - [E^1]^{\mathrm{T}}]\{u_h(\xi)\} + \xi^2\{F^{\mathrm{b}}(\xi)\} + \xi\{F^t(\xi)\} = \{0\} \quad (90)$$

For body loads with a variation in the ξ direction proportional to ξ^b, as in Eq. (58), the body load mode is

$$\{\phi_b\} = [(b+2)^2[E^0] + (b+2)[[E^0] + [E^1]^{\mathrm{T}} - [E^1]] - [[E^2] - [E^1]^{\mathrm{T}}]]^{-1}\{-F_b\} \quad (91)$$

while for side-face loads with a variation in the ξ direction proportional to ξ^t (Eq. (63)), the side-load deformation mode is

$$\{\phi_t\} = [(t+1)^2[E^0] + (t+1)[[E^0] + [E^1]^{\mathrm{T}} - [E^1]] - [[E^2] - [E^1]^{\mathrm{T}}]]^{-1}\{-F_t\} \quad (92)$$

Apart from these minor changes to the coefficient matrices, all other equations remain the same, and computer implementation remains simple.

6 Discussion

In contrast to the finite element method, the scaled boundary finite-element method is a semi-analytical technique. The solution is analytical in the radial direction, but is based on shape functions in the circumferential direction. Equilibrium in the radial direction and boundary conditions along the side-faces are closely satisfied, while equilibrium in the circumferential direction is satisfied in the finite element sense. If side-faces are present, the two side-faces intersect at the scaling centre, and since the boundary conditions on the two side-faces may be distinct, there may be a singularity or discontinuity in the stress field at this centre. The scaled boundary finite-element method is able to reproduce this feature exactly.

The finite element method generally only satisfies internal equilibrium and traction boundary conditions in the limit as the element size becomes zero. The boundary element method satisfies internal equilibrium, but only satisfies boundary conditions in the limit. However, although the scaled boundary finite-element method tends to the correct solution in the limit (like the finite element method), side-face boundary conditions and equilibrium requirements in the radial direction are closely satisfied due to the application of analytical solution techniques. Consequently, to take full advantage of the method the scaling centre and side-faces should be strategically located. A sub-structuring approach can be employed to achieve this.

Since the scaled boundary finite-element method finds the stiffness of a domain relative to nodes located along its boundary, such domains can be assembled together as 'super-elements' before the nodal displacements are computed. This is illustrated in Fig. 5. Once the boundary displacements have been found, internal displacements and stresses for each domain can be computed. Each domain has its own scaling centre and (possibly) two side-faces. Since any number of super-elements can be assembled together, they can be positioned to optimise the unique properties of these features. Scaling centres should be located at discontinuities in boundary geometry or boundary conditions, while the true boundary of the structure should be modelled as far as possible with side-faces. The scaled boundary finite-elements can be positioned within the structure to connect the various domains.

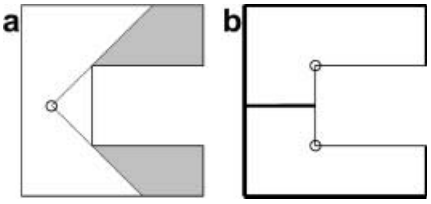

Fig. 5. A domain which must be sub-structured. **a** Regions of boundary not visible from potential scaling centre. **b** Discretisation with two sub-domains, heavy lines represent discretised boundaries

These features are illustrated with examples in the next section. Consistent with the goal of the paper outlined in the Introduction, simple examples demonstrating the salient features and high accuracy are addressed.

7 Examples

7.1 Example 1 – flexible circular footing on a half-space

The first example is a flexible circular footing on a half-space, illustrated in Fig. 6a. Due to the semi-infinite nature of the problem, sensible comparisons with finite element analysis are difficult, since the accuracy of such calculations depends on the treatment of the unbounded domain. The scaled boundary finite-element method, on the other hand, handles unbounded domains without any special treatment. Fortunately, an exact solution for this problem is available, and so the accuracy of the scaled boundary finite-element analysis is shown through comparison with this solution, rather than with another numerical solution.

The axisymmetric domain is analysed as two separate subdomains, one bounded and one unbounded. The line separating the two subdomains is discretised by scaled boundary finite-elements. The scaling centre for both the bounded and unbounded domains is selected at the centre of the footing. As the surface of the half-space is a side-face, no spatial discretisation applies to this line. Likewise, the footing lies on a side-face of the bounded domain, and again no spatial discretisation applies. The footing load is prescribed as a traction on this side-face.

Three meshes of increasing accuracy are used. The elements are three-noded quadratic line elements. The mesh designated as 'coarse' consists of just two of these elements, and is illustrated in Fig. 6b. The mesh designated as 'medium' consists of four of these elements, and is formed by a binary subdivision of the coarse mesh, while the mesh designated as 'fine' consists of

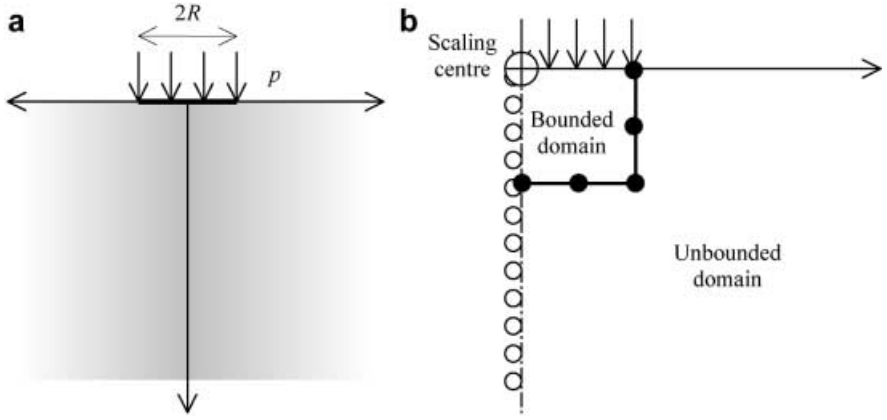

Fig. 6. **a** Layout for Examples 1 and 2; **b** coarse mesh for Example 1

eight elements, and is formed by binary subdivision of the medium mesh.

The results of the analyses are shown in Table 1. The dimensionless displacement at the centre of the footing δ^* is related to the footing displacement δ, the shear modulus G, Poisson's ratio v, the pressure on the footing p and the footing radius R by

$$\delta^* = \frac{G}{pR(1-v)}\delta \tag{93}$$

The indicative timings are recorded in seconds on a 450 MHz Pentium III PC. Note that general purpose routines are used for solution of the eigenproblem, as no attempt has been made at this stage to optimise the performance of the program. Also, as the program has been written for the general assembly of sub-domains, no advantage is taken of the fact that the eigenproblems for the bounded and unbounded sub-domains are identical. Since most of the time is taken up in the solution of the eigenproblem, the computational times for this example (and for the second example) could be reduced by about 50% by solving the eigenproblem just once.

The error estimator η^* shown in the table is of the Zienkiewicz-Zhu (1987) energy norm type. The value of this estimator may be interpreted as an approximate weighted root-mean-square of the error in the stress field. The error is computed over the entire unbounded domain semi-analytically. The procedure used to evaluate this error estimator is described in detail by Deeks and Wolf (2002).

Table 1. Results for Example 1, flexible circular footing on half-space

Mesh	DOF	Time	Displacement δ^*	Error estimation η^* (%)
Coarse	9	0.06	0.992	10.2
Medium	17	0.30	0.998	5.1
Fine	33	1.71	0.999	2.0
Exact			1.000	

The table shows that excellent accuracy of displacements and stresses are obtained with the medium mesh. The contour plots of vertical stress (Fig. 7) demonstrate the accuracy of the computed stress distributions, and indicate that even the coarse mesh gives reasonable results. The accuracy of the fine mesh is quite remarkable, and is achieved in less than two seconds. The stress is rendered dimensionless by division by the pressure on the footing, p.

7.2
Example 2 – rigid circular footing on a half-space

The second example is virtually identical to the first. The only difference lies in the stiffness of the footing, which is taken to be perfectly rigid in this case. The footing is also assumed to be rough, implying the soil does not slip horizontally relative to the footing.

The numerical solution of this problem is much more challenging than the first example. Not only is the domain unbounded, but the exact stress field has a stress singularity at the edge of the footing. Fortunately, an analytical solution is available for comparison purposes. Accurate analysis using the finite element method is difficult to achieve.

Since the stress singularity does not occur on the axis of symmetry, it is not possible to locate the scaling centre at the singularity in this case. However, the results of the example are of interest as they demonstrate the rate of convergence of the scaled boundary finite-element method around points of stress singularity located away from the scaling centre, which is selected in the same location as in Example 1.

The same meshes are used as for the first example, except an additional 'very fine' mesh is formed by binary

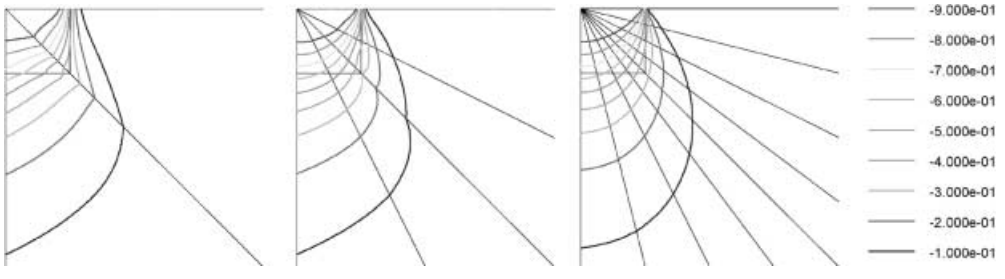

Fig. 7. Contours of vertical stress under the flexible circular footing of Example 1

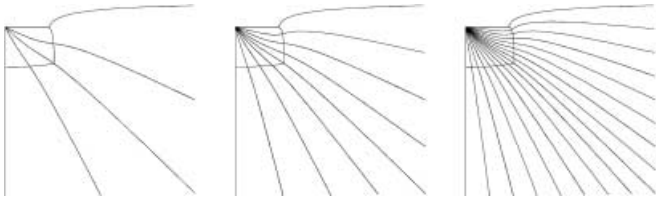

Fig. 8. Displacements of the half-space under the rigid circular footing of Example 2

Table 2. Results for Example 2, rigid circular footing on half-space

Mesh	DOF	Time	Displacement δ^*	Error estimator η^* (%)
Coarse	8	0.05	1.080	15.3
Medium	16	0.27	0.978	10.8
Fine	32	1.62	0.913	7.8
Very fine	64	11.98	0.874	4.8
Exact			0.785	

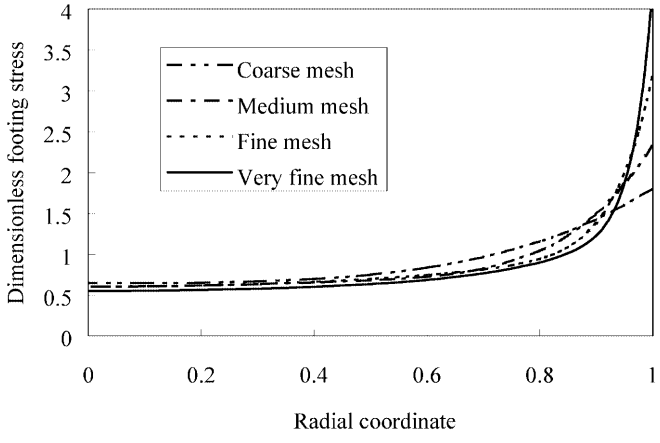

Fig. 9. Vertical stress under the rigid circular footing of Example 2

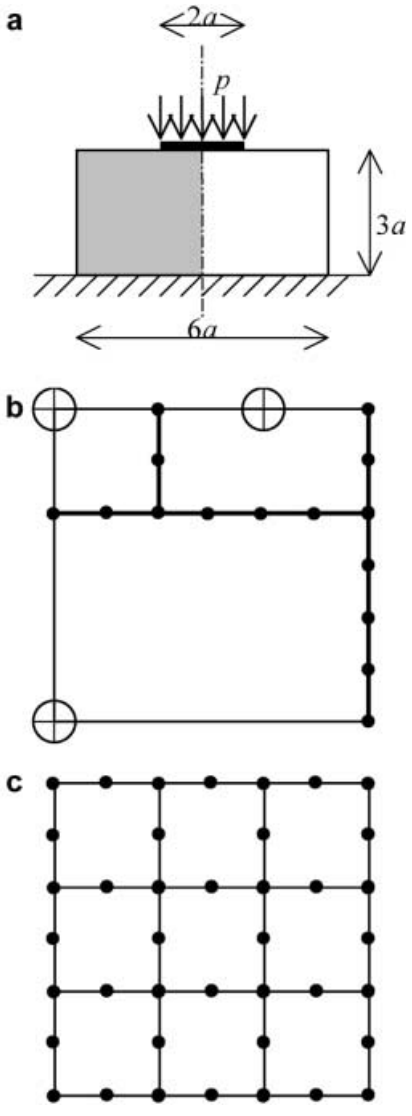

Fig. 10. **a** Layout for Examples 3 and 4; **b** coarse scaled boundary finite-element mesh with scaling centres of three subdomains; **c** coarse finite element mesh

subdivision of the fine mesh. As with the first example, only the boundary between the bounded and unbounded domains is discretised. The computed displacement fields for the first three meshes are illustrated in Fig. 8. A sharp discontinuity in slope at the edge of the footing is evident.

The recorded results are presented in Table 2, where the number of degrees of freedom, the computational time, the dimensionless displacement and the value of the error estimator are tabulated for each mesh. Convergence is not so rapid for this example, particularly for the displacement. However, the stress field converges relatively quickly (particularly when compared with the finite element analysis of a rigid bearing plate presented in Example 4). The convergence of the vertical stress under the footing is illustrated in Fig. 9. The stress is again rendered dimensionless by division by p.

7.3
Example 3 – Flexible plate on a bearing block

Examples 3 and 4 illustrate the benefits that can be achieved by taking advantage of the properties of the scaling centre and the side-faces. In Example 3 a flexible bearing plate exerts a uniform vertical load on a rectangular bearing block, which is rigidly supported at its base (Fig. 10). The problem is treated as one of plane stress, and advantage taken of the vertical axis of symmetry. An analytical solution is not available for this example, but since the domain is bounded, finite element analysis can be performed readily.

To fully exploit the special features of the scaled boundary finite-element method, the domain is broken into three subdomains, as illustrated in Fig. 10. This permits a scaling centre to be positioned at the point at which the vertical stress is discontinuous, that is at the edge of the flexible bearing plate, along with two of the boundary points at which sharp corners are present. The flexible bearing plate is modelled as a side-face with prescribed traction boundary conditions. Other side-faces are used to allow traction free boundaries to be modelled with minimal error. The coarse mesh of elements making up the model is also shown in Fig. 10. Medium and fine meshes are generated by binary

Table 3. Results for Example 3, flexible plate on a bearing block

Mesh	Finite element method				Scaled boundary finite-element method			
	DOF	Time	$\delta*$	$\eta*$ (%)	DOF	Time	δ^*	η^* (%)
Coarse	66	0.038	−2.284	17.36	22	0.416	−2.294	3.71
Medium	240	0.155	−2.289	8.85	44	2.595	−2.294	0.80
Fine	912	0.740	−2.293	4.39	88	17.770	−2.294	0.19
Very fine	55680	1369.146	−2.294	0.55				

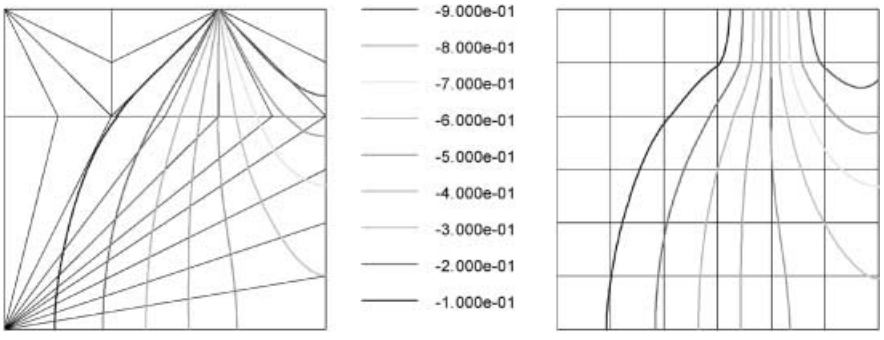

Fig. 11. Vertical stress contours for Example 3 obtained with the medium meshes: left – scaled boundary finite-element method; right – finite element method

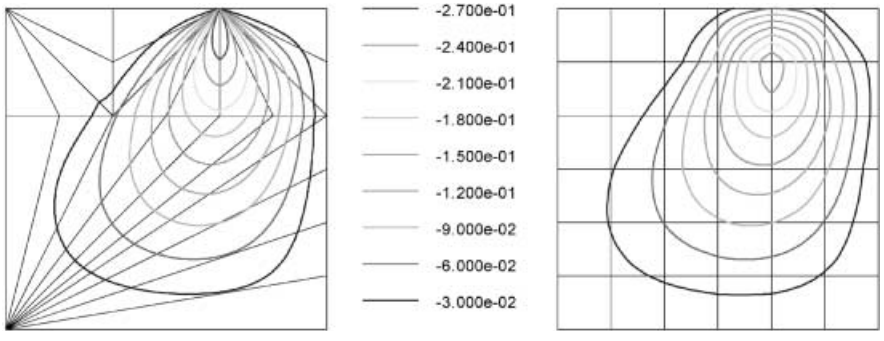

Fig. 12. Shear stress contours for Example 3 obtained with the medium meshes: left – scaled boundary finite-element method; right – finite element method

subdivision of this initial mesh. Three-noded quadratic line elements are used.

The finite element models are formed using eight-noded quadratic elements. The rigid bearing plate is modelled by prescribing the vertical displacements of the nodes that fall beneath the plate. The initial coarse mesh is shown in Fig. 10. Medium, fine and very fine meshes are generated by binary subdivision. Poisson's ratio is taken as 0.3, and the dimensionless vertical displacement of the centre of the plate δ^* is related to the actual displacement δ, the Young's modulus of the block E, the pressure on the plate p and the dimension a indicated in Fig. 10 by

$$\delta^* = \frac{E}{pa}\delta \tag{94}$$

The relative performance of the methods with the set of meshes described above is presented in Table 3. Although the time required by the scaled boundary finite-element method is larger for a given number of degrees of freedom, the accuracy (measured by the Zienkiewicz and Zhu (1987) style stress error estimator η^*) achieved even with very few degrees of freedom is quite remarkable. Even the fine mesh of the finite element method fails to achieve results as accurate as the coarse mesh of the scaled boundary finite-element method, although the analysis takes almost twice as long. The very fine mesh of the finite element method achieves results comparable to the medium mesh of the scaled boundary finite-element method, but takes about 500 times as long. This huge increase in time is attributable to the stiffness matrix for the 55 680 degree of freedom model expanding out of physical memory and into virtual memory, and a machine with more physical memory may not suffer so heavy a penalty.

The accuracy of the scaled boundary finite-element method can be understood when the stress contour plots of the medium scaled boundary finite-element model (44 degrees of freedom, 0.8% error estimate) are compared with those of the corresponding finite element model (240 degrees of freedom, 8.8% error estimate). The contours of vertical stress are shown in Fig. 11. (All stress components are rendered dimensionless by division by the pressure on the footing.) The scaled boundary finite-element method is able to accurately model the stress discontinuity at the edge of the flexible bearing plate, allowing the prescribed surface tractions to be attained both under the bearing plate and along the free surfaces of the block. In contrast, the finite element method is unable to represent this discontinuity, and equilibrium is violated dramatically in the vicinity of the edge plate. This effect is shown graphically by the distortion of the stress bulbs illustrated in Fig. 11.

Figure 12 shows the shear stress contours for the same pair of models. While the scaled boundary finite-element model is able to accurately represent the discontinuity in shear stress at the edge of the footing, the finite element

Table 4. Results for Example 4, rigid place on a bearing block

Mesh	Finite element method				Scaled boundary finite-element method			
	DOF	Time	δ^*	η^* (%)	DOF	Time	δ^*	η^* (%)
Coarse	63	0.04	1.838	29.78	21	0.40	1.939	5.03
Medium	235	0.16	1.888	21.85	43	2.60	1.941	1.17
Fine	903	0.72	1.914	15.33	87	17.91	1.941	0.25
Very fine	55615	1386.72	1.938	5.38				

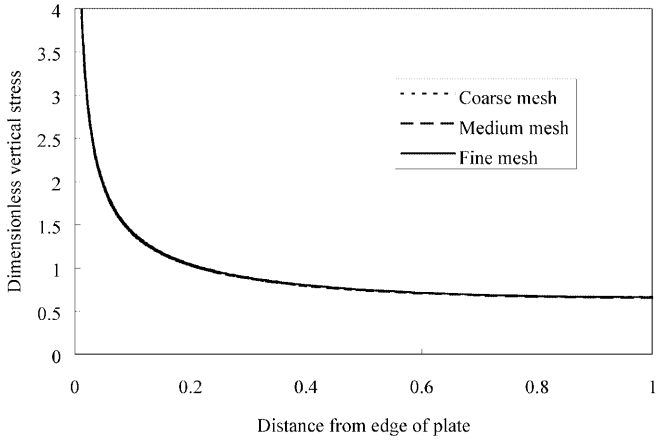

Fig. 13. Vertical stress computed under the rigid bearing plate of Example 4 (scaled boundary finite-element method)

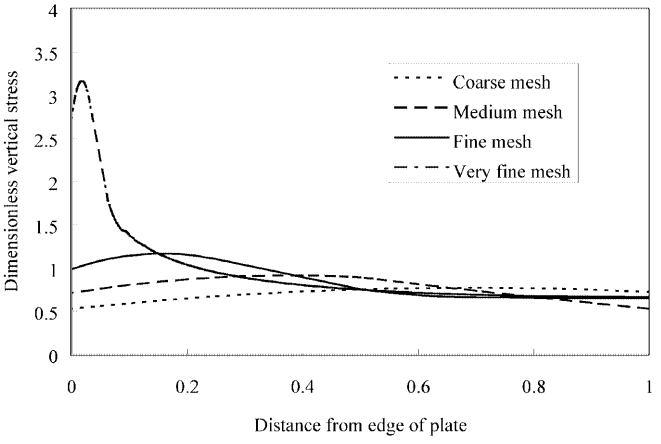

Fig. 14. Vertical stress computed under the rigid bearing plate of Example 4 (finite element method

model does not, and in fact indicates the maximum shear stress to occur some way below the top of the block.

7.4
Example 4 – Rigid plate on a bearing block

The final example is similar to Example 3, except that the bearing plate is now considered to be rigid. This change is implemented by placing a prescribed displacement boundary condition on the side-face under the plate in the scaled boundary finite-element models, and on the nodes under the plate in the finite element models, in contrast with the prescribed traction boundary conditions used in Example 3.

This causes the exact stress field to become singular under the edge of the bearing plate. The results of the analyses are presented in Table 4. The effect of the singularity on the accuracy of the scaled boundary finite-element method is minor. However, the accuracy of the finite element method suffers considerably. For this example even the very fine mesh of the finite element method is less accurate than the coarse mesh of the scaled boundary finite-element method.

The energy norm of the error (as evaluated by the error estimator) is a weighted average of the error over the entire domain. When the vertical stress immediately beneath the bearing plate is examined in detail, the performance of the scaled boundary finite-element method is seen to be greatly superior. Figure 13 (in which the vertical stress is rendered dimensionless by division by the pressure on the footing) indicates that the three scaled boundary finite-element meshes give virtually the same result, showing there is negligible error in even the coarsest scaled boundary finite-element mesh in this region of high interest. In contrast, Fig. 14 indicates that even the very fine finite element mesh yields a poor approximation, while an inexperienced analyst might miss the singularity all together on observing the results for the first three finite element meshes.

8
Conclusions

This paper presents a new virtual work derivation of the scaled boundary finite-element method. The formulation establishes all the equations necessary for solution directly from the virtual work statement, and leads to a modal interpretation of the solution process, where the solution is found as a combination of displacement modes, each of which closely satisfies equilibrium in the radial direction. The participation of each mode in the solution is determined by the application of boundary conditions. The formulation also permits side-face loads and body loads to be included in a simple manner. A new version of the scaled boundary finite-element equation in displacement is established for axisymmetric situations. This treatment of axisymmetry allows simpler implementation within a general scaled boundary finite-element computer program than existing methods.

The significance of the scaling centre and its use in allowing accurate analysis of stress discontinuities and singularities is discussed, together with the use of side-faces to allow accurate analysis of boundary tractions. The paper illustrates how the geometric limitation of the scaled boundary finite-element method (namely that the complete boundary be visible from a single point) may be overcome by the use of sub-structuring.

Four examples are presented to show how well the scaled boundary finite-element method performs in practice. The first two employ a combination of bounded and unbounded subdomains to solve an unbounded problem, and demonstrate the capability of the method to deal with unbounded problems. The second example includes a stress singularity not located at the scaling centre, and indicates that the scaled boundary finite-element method converges rapidly in the finite element sense around such points. The third and fourth examples illustrate how advantage can be taken of the ability of the scaling centre and the side-boundaries to accurately model prescribed boundary tractions and displacements. The third example contains a discontinuity in the boundary traction, which is accurately modelled by locating a scaling centre at this point. Similarly, the fourth example demonstrates the ability of the scaled boundary finite-element method to model stress singularities located at the scaling centre.

The performance of the scaled boundary finite-element method is compared with the standard finite element method for the third and fourth examples (since these are bounded). Despite the use of rather primitive general purpose eigensolution routines in the implementation of the scaled boundary finite-element method, the scaled boundary finite-element method outperforms the standard finite element method for comparable computational time in terms of overall accuracy, number of degrees of freedom, and qualitative accuracy in the regions of high interest (the points of stress singularity and discontinuity).

Overall the paper shows that the novel semi-analytical scaled boundary finite-element method can be derived in a similar manner to the standard finite element method, and has the potential to be used to great advantage in problems of elastostatics.

Appendix A – Vector and matrix definitions for plane stress, plane strain and axisymmetry

In the case of plane stress and plane strain, the displacement field has two components, displacement in the x-direction (u_x) and displacement in the y-direction (u_y).

$$\{u\} = \begin{Bmatrix} u_x \\ u_y \end{Bmatrix} \tag{A1}$$

Stress and strain have three independent components.

$$\{\sigma\} = \begin{Bmatrix} \sigma_x \\ \sigma_y \\ \tau_{xy} \end{Bmatrix} \tag{A2}$$

$$\{\varepsilon\} = \begin{Bmatrix} \varepsilon_x \\ \varepsilon_y \\ \gamma_{xy} \end{Bmatrix} \tag{A3}$$

The linear operator relating strain and displacement is

$$[L] = \begin{bmatrix} \frac{\partial}{\partial x} & 0 \\ 0 & \frac{\partial}{\partial y} \\ \frac{\partial}{\partial y} & \frac{\partial}{\partial x} \end{bmatrix} \tag{A4}$$

The elasticity matrix for plane stress is

$$[D] = \frac{E}{1-v^2}\begin{bmatrix} 1 & v & 0 \\ v & 1 & 0 \\ 0 & 0 & \frac{1-v}{2} \end{bmatrix} \tag{A5a}$$

and for plane strain

$$[D] = \frac{E}{(1+v)(1-2v)}\begin{bmatrix} 1-v & v & 0 \\ v & 1-v & 0 \\ 0 & 0 & \frac{(1-2v)}{2} \end{bmatrix} \tag{A5b}$$

where E and v are Young's modulus and Poisson's ratio respectively.

In the case of axisymmetry (when both load and displacement are axisymmetric) the displacement field still has two components (in the r and z directions), but stress and strain have an additional component in the circumferential θ direction.

$$\{\sigma\} = \begin{Bmatrix} \sigma_r \\ \sigma_z \\ \sigma_\theta \\ \tau_{rz} \end{Bmatrix} \tag{A6}$$

$$\{\varepsilon\} = \begin{Bmatrix} \varepsilon_r \\ \varepsilon_z \\ \varepsilon_\theta \\ \gamma_{rz} \end{Bmatrix} \tag{A7}$$

The linear operator is

$$[L] = \begin{bmatrix} \frac{\partial}{\partial r} & 0 \\ 0 & \frac{\partial}{\partial z} \\ \frac{1}{r} & 0 \\ \frac{\partial}{\partial z} & \frac{\partial}{\partial r} \end{bmatrix} \tag{A8}$$

and the elasticity matrix is

$$[D] = \frac{E}{(1+v)(1-2v)}\begin{bmatrix} 1-v & v & v & 0 \\ v & 1-v & v & 0 \\ v & v & 1-v & 0 \\ 0 & 0 & 0 & \frac{(1-2v)}{2} \end{bmatrix} \tag{A9}$$

Appendix B – Transformation to the scaled boundary coordinate system

The scaling equations relating the Cartesian coordinate system to the scaled boundary coordinate system are

$$x = x_0 + \xi x_s(s) \tag{B1a}$$

$$y = y_0 + \xi y_s(s) \tag{B1b}$$

Derivatives in the scaled boundary coordinate system can be related to derivatives in the Cartesian coordinate system using the Jacobian matrix.

$$\begin{Bmatrix} \frac{\partial}{\partial \xi} \\ \frac{\partial}{\partial s} \end{Bmatrix} = \begin{bmatrix} \frac{\partial x}{\partial \xi} & \frac{\partial y}{\partial \xi} \\ \frac{\partial x}{\partial s} & \frac{\partial y}{\partial s} \end{bmatrix} \begin{Bmatrix} \frac{\partial}{\partial x} \\ \frac{\partial}{\partial y} \end{Bmatrix} \tag{B2}$$

Taking derivatives of Eqs. (B1) with respect to ξ and moving the ξ term to the left-hand side

$$\begin{Bmatrix} \frac{\partial}{\partial \xi} \\ \frac{1}{\xi}\frac{\partial}{\partial s} \end{Bmatrix} = \begin{bmatrix} x_s(s) & y_s(s) \\ x_s(s)_{,s} & y_s(s)_{,s} \end{bmatrix} \begin{Bmatrix} \frac{\partial}{\partial x} \\ \frac{\partial}{\partial y} \end{Bmatrix} \tag{B3}$$

Inverting yields

$$\begin{Bmatrix} \frac{\partial}{\partial x} \\ \frac{\partial}{\partial y} \end{Bmatrix} = \frac{1}{|J|} \begin{bmatrix} y_s(s)_{,s} & -y_s(s) \\ -x_s(s)_{,s} & x_s(s) \end{bmatrix} \begin{Bmatrix} \frac{\partial}{\partial \xi} \\ \frac{1}{\xi}\frac{\partial}{\partial s} \end{Bmatrix} \tag{B4}$$

where the Jacobian at the boundary ($\xi = 1$) is

$$|J| = x_s(s)y_s(s)_{,s} - y_s(s)x_s(s)_{,s} \tag{B5}$$

For plane stress and plane strain problems the incremental "volume" is

$$\mathrm{d}V = |J|\xi \,\mathrm{d}\xi \,\mathrm{d}s \tag{B6}$$

If the linear operator is decomposed as

$$[L] = [L^1]\frac{\partial}{\partial x} + [L^2]\frac{\partial}{\partial y} \tag{B7}$$

using Eq. (B4) yields

$$\begin{aligned}[L] &= \frac{1}{|J|}\left[[L^1]\left(y_s(s)_{,s}\frac{\partial}{\partial \xi} - y_s(s)\frac{1}{\xi}\frac{\partial}{\partial s}\right)\right. \\ &\quad \left. + [L^2]\left(-x_s(s)_{,s}\frac{\partial}{\partial \xi} + x_s(s)\frac{1}{\xi}\frac{\partial}{\partial s}\right)\right] \\ &= [b^1(s)]\frac{\partial}{\partial \xi} + [b^2(s)]\frac{1}{\xi}\frac{\partial}{\partial s}\end{aligned} \tag{B8}$$

where

$$[b^1(s)] = \frac{1}{|J|}\left[[L^1]y_s(s)_{,s} - [L^2]x_s(s)_{,s}\right] \tag{B9}$$

$$[b^2(s)] = \frac{1}{|J|}\left[-[L^1]y_s(s) + [L^2]x_s(s)\right] \tag{B10}$$

In the same way, for axisymmetric problems the scaling centre is limited to being on the axis of symmetry, and the scaling equations relating the cylindrical coordinate system to the scaled boundary coordinate system are

$$r = \xi r_s(s) \tag{B11a}$$

$$z = z_0 + \xi z_s(s) \tag{B11b}$$

In this case

$$|J| = r_s(s)z_s(s)_{,s} - z_s(s)r_s(s)_{,s} \tag{B12}$$

and

$$\mathrm{d}V = 2\pi r_s|J|\xi^2 \,\mathrm{d}\xi \,\mathrm{d}s \tag{B13}$$

If the linear operator is decomposed as

$$[L] = [L^1]\frac{\partial}{\partial r} + [L^2]\frac{\partial}{\partial z} + [L^3]\frac{1}{r} \tag{B14}$$

then

$$[L] = [b^1(s)]\frac{\partial}{\partial \xi} + [b^2(s)]\frac{1}{\xi}\frac{\partial}{\partial s} + [b^3(s)]\frac{1}{\xi} \tag{B15}$$

where

$$[b^1(s)] = \frac{1}{|J|}\left[[L^1]z_s(s)_{,s} - [L^2]r_s(s)_{,s}\right] \tag{B16}$$

$$[b^2(s)] = \frac{1}{|J|}\left[-[L^1]z_s(s) + [L^2]r_s(s)\right] \tag{B17}$$

$$[b^3(s)] = \frac{1}{r_s(s)}[L^3] \tag{B18}$$

References

Benzley SE (1974) Represenation of singularities with isoparametric finite elements. Int. J. Num. Meth. Eng. 8: 537–545

Bettess P (1977) Infinite elements. Int. J. Num. Meth. Eng. 11: 1271–1290

Deeks AJ, Wolf JP (2002) Stress recovery and error estimation for the scaled boundary finite-element method. Int. J. Num. Meth. Eng.

Song Ch, Wolf JP (1997) The scaled boundary finite-element method – alias consistent infinitesimal finite-element cell method – for elastodynamics. Comp. Meth. Appl. Mech. Eng. 147: 329–355

Song Ch, Wolf JP (1999) Body loads in scaled boundary finite-element method. Comp. Meth. Appl. Mech. Eng. 180: 117–135

Wolf JP, Song Ch (1996a) Consistent infinitesimal finite-element cell method: three dimensional vector wave equation. Int. J. Num. Meth. Eng. 39: 2189–2208

Wolf JP, Song Ch (1996b) Finite-Element Modelling of Unbounded Media. John Wiley and Sons, Chichester

Wolf JP, Song Ch (2001) The scaled boundary finite-element method – a fundamental solution-less boundary-element method. Comp. Meth. Appl. Mech. Eng. 190: 5551–5568

Zienkiewicz OC, Zhu JZ (1987) A simple error estimator and adaptive procedure for practical engineering analysis. Int. J. Num. Meth. Eng. 24: 337–357

Zienkiewicz OC (1977) The Finite Element Method. 3rd ed, McGraw Hill, London